Applied Clay Science 276 (2025) 107915

Contents lists available at ScienceDirect

Applied Clay Science

journal homepage: www.elsevier.com/locate/clay

Research Paper

Bentonite mass loss in fractured crystalline rock quantified from CT scans using digital rock physics and machine learning: case study from the Grimsel Test Site (Switzerland)☆

Saeid Sadeghnejad[a], Sarah Hupfer[a], Janis Pingel[a], Bill Lanyon[b], Raphael Schneeberger[c], Ingo Blechschmidt[c], Ursula Alonso[d], Wolfgang Hauser[e], Stephanie Kraft[e], Horst Geckeis[e], Thorsten Schäfer[a,*]

[a] *Institute for Geoscience, Applied Geology, Friedrich Schiller University Jena, Jena, Germany*
[b] *Fracture Systems Ltd, St. Ives, United Kingdom*
[c] *Nagra (National Cooperative for the Disposal of Radioactive Waste), Wettingen, Switzerland*
[d] *Physico-Chemistry of Actinides and Fission Products Unit, CIEMAT, Madrid, Spain*
[e] *Karlsruhe Institute of Technology, Institute for Nuclear Waste Disposal (INE), Eggenstein-Leopoldshafen, Germany*

ARTICLE INFO

Keywords:
Fracture aperture distribution
Bentonite erosion
FEBEX bentonite
CT scan
Digital twin
Machine learning
Uncertainty analysis

ABSTRACT

Bentonite plays a critical role in engineered barrier systems designed for radioactive waste storage in geological repositories especially in crystalline formations. Ensuring its long-term stability under realistic hydrogeochemical conditions is vital for evaluating the safety of these repositories. This study investigated the influence of controlled water flow in a shear zone on the erosion of bentonite through a 4.5-year Long-Term In-Situ Test (LIT) at the Grimsel Test Site, Switzerland. Compacted Ca-Mg-type FEBEX bentonite rings (with 90 % montmorillonite content) were positioned in-situ in an emplacement borehole intersecting a water-conducting shear zone providing direct contact with low-mineralized glacial meltwater. X-ray computed tomography scanning, along with digital rock physics methods, were used to quantify bentonite mass loss and the contact shear zone aperture distribution on over-cored LIT samples. A Random Forest classifier, a machine learning technique, was used for segmentation, which enabled more precise quantification of bentonite mass loss and improved fault characterization. This approach used multiphase segmentation, allowing accurate distinction between different material phases in the cored interval, which is essential for resolving complex interactions in heterogeneous systems. The selection of the correct region of interest was crucial for minimizing segmentation errors and improving mass loss quantification by reducing interferences from non-relevant structures. The aperture distribution between the three boreholes over-cored within the shear zone was evaluated with a mean thickness of 2.90 ± 1.09 mm (2σ). Furthermore, the bentonite mass loss was computed from the scanned images and compared with mobilised montmorillonite colloid masses, continuously sampled in the water from observation boreholes (0.11–0.12 m and 6 m distance) measured by inductively coupled plasma mass spectrometry (ICP-MS) and laser-induced breakdown detection (LIBD) techniques. The data evaluation of both techniques used in this study provided erosion rates <2 kg/m^2/y, which are at least two orders of magnitude below the mass loss assessment rates of 500 to 1500 kg/m^2/y defined by safety case considerations of the Swedish Nuclear Fuel and Waste Management Company (Svensk Kärnbränslehantering Aktiebolag, SKB) and the Finnish company POSIVA handling the final disposal of the spent nuclear fuel generated by its owners, the nuclear plant operators Teollisuuden Voima and Fortum. The creation of a digital twin model for the bentonite-water-shear zone system provided new insights into the erosion processes showing inhomogeneous erosion in contact with real fracture geometries.

☆ This article is part of a Special issue entitled: 'Clay Conf. Hannover 2024' published in Applied Clay Science.

* Corresponding author.
E-mail address: thorsten.schaefer@uni-jena.de (T. Schäfer).

https://doi.org/10.1016/j.clay.2025.107915
Received 17 April 2025; Received in revised form 17 June 2025; Accepted 18 June 2025

1. Introduction

The concept of a passive multi-barrier system in a geological disposal facility is generally considered for the long-term isolation of radioactive waste from the biosphere (Sellin and Leupin, 2013). Beside the host rock as natural geological barrier, the engineered barrier system (EBS) enhances safety through different materials such as corrosion-resistant canisters or low-permeable buffer material between waste packages and host rock. The buffer is often composed of bentonite, with high montmorillonite content, sometimes mixed with additional materials e.g., quartz sand. The key properties of a bentonite-based buffer are the low hydraulic permeability, the self-sealing ability due to the swelling pressure, and the long-term mineralogical stability (Sellin and Leupin, 2013). Groundwater uptake will yield swelling of bentonite buffers and a swelling pressure will develop due to the space restrictions (Gens et al., 2009). Even if host rock fractures are intersecting the bentonite buffer it will continue to swell and expand into the open space potentially formed by these fractures. The formation and release of montmorillonite colloids (Missana et al., 2003) in response to swelling could form a transport pathway for strong-sorbing radionuclides under certain geochemical conditions (Kretzschmar and Schäfer, 2005; Quinto et al., 2017; Schäfer et al., 2012). These conditions of low-mineralized groundwater are typically found in meteoric or glacial meltwater. Below the so-called critical coagulation concentration (Birgersson et al., 2011; Seher et al., 2020), individual montmorillonite layers may swell sufficiently to give the clay/water system a sol character, i.e., form montmorillonite colloidal particles. The critical coagulation concentration (CCC) is determined in monovalent systems (e.g. Na) and used as a pessimistic concentration limit for spontaneous clay colloid release. Bentonite colloids released would decrease the total buffer mass.

A Derjaguin-Landau-Verwey-Overbeek-theory (DLVO)-based force-balance model for clay layers initially valid only for sodium can be used to calculate the swelling and advective mass loss of montmorillonite in fractures as parallel plates or with different roughness simulated by aperture standard deviations and correlation lengths (Huber et al., 2021; Liu et al., 2009).

The CFM (Colloid Formation and Migration) Project at the Grimsel Test Site and its LIT (Long term in-situ Test) erosion experiment gives the opportunity to check, under realistic and controlled low ionic strength water conditions, the bentonite release rates and mass loss via (a) colloid monitoring in the water of a natural fracture zone (MI shear zone) and (b) the post-mortem analysis of the over-cored experimental set-up via analysis of the computer-tomography (CT) data (Schlickenrieder et al., 2017). The focus of this work is on the CT data post-processing by means of Digital Rock Physics (DRP), machine learning-based (ML) segmentation, and finally the estimate of bentonite mass loss in comparison to the groundwater colloid analysis.

The DRP workflow involves using digital representations of samples (i.e., digital twin) to simulate physical phenomena (Sadeghnejad et al., 2023; Tian et al., 2021). The process usually starts with imaging a rock sample using X-ray computed tomography (CT) followed by image processing (e.g., denoising) and segmentation. Segmentation is a critical step in the DRP workflow (Moslemipour et al., 2025; Sadeghnejad et al., 2021). The traditional segmentation approach usually relies on manual interaction and implementing thresholding-based algorithms (Huang et al., 2021; Kapur et al., 1985; Otsu, 1979; Tsai, 1985; Wang and Haralick, 1984), cluster analysis, and boundary detection (Vincent and Soille, 1991). However, several challenges arise in multiphase segmentation, where more than two target phases exist in an image. These challenges include variations in greyscale intensity, noise, and phase boundaries that makes segmentation more challenging. Additionally, manual segmentation of large image datasets is time-consuming and subjective to user bias. Thus, ML-based approaches can be implemented to enhance accuracy and reproducibility.

Recent advancements in nuclear waste disposal shifted toward the data-driven ML approaches (Hu and Pfingsten, 2023; Hu et al., 2021) including the image segmentation task. While supervised deep learning approaches, such as Convolutional Neural Networks (CNNs) have gained prominence for their ability to automatically extract image features and achieve high classification accuracy (Niu et al., 2020; Tang et al., 2022), shallow learning methods, such as Random Forest (RF), remain highly effective, particularly in scenarios with limited training data (Reinhardt et al., 2022). This makes them particularly suitable for applications where acquiring large, annotated datasets is challenging. Moreover, unsupervised segmentation techniques such as K-means (Dhanachandra et al., 2015), Gaussian Mixture Models (Lee and Lee, 2010), and autoencoder-based deep clustering (Yu et al., 2018) can be used when labelled data is not available. While these methods are generally simpler than supervised approaches, they often struggle capturing complex spatial patterns.

This study presents an application of DRP to quantify bentonite mass loss and analyze shear zone properties in the Long-term In-situ Test (LIT) at the Grimsel Test Site (GTS), Switzerland. By integrating CT scanning with RF classifier as a segmentation tool, precise quantification of bentonite mass loss as well as fault aperture distribution is achieved, overcoming the limitations of traditional thresholding methods. The development of a digital twin model for the bentonite-shear zone system provided insights into erosion dynamics and hydro-mechanical interactions within fractured crystalline rocks.

2. Material & methods

2.1. The Grimsel Test Site (GTS)

The Grimsel Test Site (GTS) is an underground research laboratory located in the crystalline rocks of the central Swiss Alps, approximately 350 to 520 m below ground and operated by the Swiss National Cooperative for the Disposal of Radioactive Waste (Nagra) (Schneeberger et al., 2019). Two main aspects render the Grimsel Test Site suitable for testing selected aspects on the evolution of a geological disposal facilities especially the impact of glaciation scenarios on the EBS integrity. Firstly, it is fractured crystalline rock. This implies parts characterized by zones of higher and lower transmissivity. This combination in turn results in a combination of advective transport dominated sections juxtaposed to molecular diffusion dominated sections. Secondly, the hydraulic setting is dominated by low-mineralized meteoric water with alkaline pH conditions (Schneeberger et al., 2019) and therefore an analogue to possible glacial water ingress related to future glaciations.

2.2. LIT experiment at GTS (design and monitoring system)

The LIT bentonite erosion experiment was initiated as part of the Colloid Formation and Migration (CFM) project at the GTS using the Migration (MI) shear zone (Bossart and Mazurek, 1991). The MI shear zone is a steeply SSE dipping complex geological structure exhibiting both brittle and ductile deformation features (Alexander et al., 2001). The shear zone can be conceptualized as a braided system of fault zones filled with cohesionless fault gouge, which forms permeable groundwater pathways. The individual faults vary in thickness from a few millimetres to several centimetres, and their porosity ranges from 10 % to 40 % (Reiche et al., 2016). These high-porosity zones increase the hydraulic conductivity of the shear zone and thus contribute to the transport of water and colloidal particles. The overall fault architecture with braided fault gouge zone is also seen in the hydraulic testing within the MI shear zone. Local transmissivity values range from 10^{-10} to $5{\cdot}10^{-6}$ m^2/s, while the large-scale effective transmissivity is approximately 10^{-6} m^2/s (Möri et al., 2003).

The experimental setup of LIT involved the emplacement of compacted FEBEX bentonite rings around a carbon-steel mandrill partly traced with radionuclides, synthetic clay and conservative tracers within a borehole interval about 6 m from the tunnel wall, intersecting the MI shear zone with a diameter of 86 mm and a total length of 400 mm

(Schlickenrieder et al., 2017). The test was in-situ for 4.5 years, during which the bentonite experienced swelling and erosion due to uptake of low-mineralized groundwater (ionic strength of ~2 mM and pH of 9.6 under in-situ conditions). This led to the formation of colloidal particles at the bentonite surface that can migrated through the shear zone. Throughout LIT, the chemical composition of the groundwater, the evolution of colloid concentration, and radionuclide transport were continuously monitored by sampling from near-field instrumented borehole intervals (Noseck et al., 2020; Schäfer et al., 2023). The system was equipped with three near-field monitoring boreholes and a primary water extraction point (surface packer) at the tunnel wall.

The borehole monitoring system (Fig. 1, CFM 11.001, CFM 11.002, and CFM 11.003) was designed to extract samples from the bentonite near field under minimal disturbance. The system consisted of the main borehole (CFM 06.002), where the packer system including the compacted bentonite rings was emplaced and the above-mentioned three near-field boreholes, positioned to monitor hydraulic and geochemical conditions.

Beside the three near-field observation boreholes at 0.11–0.12 m distance, the transport of colloids and radionuclides in the shear zone was monitored by a surface packer called “Pinkel” at a distance of 6 m from the source in a steady flow field. During the LIT, the flow field around the source was controlled as well as possible to simulate natural groundwater movement within the shear zone and to prevent excessive flushing of the bentonite source. The imposed low-gradient steady flow field was ideal for testing colloid migration processes as it minimises any remobilisation of colloids due to hydraulic pulses.

2.3. FEBEX bentonite & ring fabrication

The clay used for the LIT experiment is so-called FEBEX bentonite (Delavernhe et al., 2015; García-Romero et al., 2019; Lloret and Villar, 2007; Villar et al., 1998). The FEBEX bentonite is characterized by a high montmorillonite content (90 %) with the major exchangeable cations (CEC) being 24 ± 1 Na, 35 ± 3 Ca, 31 ± 3 Mg and 2.6 ± 0.4 K (all values as cmol(+)/kg), which sums up to 92.5 cmol(+)/kg cations (Torres et al., 2017). Detailed analysis of the <2 μm fraction by XRD and FT-IR revealed only traces of quartz and the clay consisted of an interstratified illite-montmorillonite mineral with 13 % of non-swellable layers (Friedrich et al., 2016) in good agreement with Cuadros and Linares (1996).

For the preparation of the LIT within the CFM project (Schlickenrieder et al., 2017) it was decided to emplace the bentonite as compacted rings similar to the so-called LOT tests at Äspö (Karnland et al., 2000). The FEBEX bentonite rings were compacted in molds by CIEMAT (Centro de Investigaciones Energéticas, Medioambientales y Tecnológicas, Spain) and had the following specifications per ring ($n = 51$): mass 178.71 ± 0.29 g, dry mass 158.22 ± 0.26 g, thickness 25.05 ± 0.11 mm, volume 95.93 ± 0.41 cm^3 and dry density 1.65 ± 0.01 Mg/m^3 (Schlickenrieder et al., 2017).

Four of the bentonite rings in the center of the source emplacement interval were traced with 10 % Zn-labelled synthetic montmorillonite (Reinholdt et al., 2001; Schlickenrieder et al., 2017). The 10 % Zn-labelled synthetic montmorillonite was mixed with 90 % FEBEX bentonite and compacted into rings by CIEMAT using the same method and equipment applied to the other twelve rings in the source. The FEBEX bentonite is according to Sánchez et al. (2006) composed of 93 ± 3 % montmorillonite, 2 ± 0.5 % quartz, 2 ± 1 % potassium feldspars, 1 ± 0.7 % plagioclase, 2 ± 0.2 % cristobalite, 1 ± 0.7 % calcite and 1.5 ± 0.1 % rhyodacitic original rock (mainly, volcanic glass). Radionuclide tracers (^{45}Ca, ^{75}Se, ^{99}Tc, ^{137}Cs, ^{241}Am, ^{233}U, ^{242}Pu & ^{237}Np) were emplaced in the central part of the source in glass vials, however this aspect of LIT is beyond the scope of this paper and discussed e.g. in Quinto et al. (2019).

2.4. Bentonite colloid monitoring in the groundwater

Water samples were taken from the monitoring interval in CFM 11.002 (0.02, 0.05 mL/min) during the first half of the LIT and then from CFM 11.003 (0.05 mL/min) during the latter half. Colloid concentrations and mean particle sizes were determined on-site in-line and off-site by Laser-Induced Breakdown Detection (LIBD) with optical data acquisition or Inductively Coupled Plasma Mass Spectrometry (ICP-MS) (Geckeis et al., 2004; Hauser et al., 2002; Scherbaum et al., 1996; Stoll et al., 2017). Based on the bulk structural formula of the FEBEX bentonite $[Si_{7.66}Al_{0.34}][Al_{2.68}Fe_{0.34}Mg_{0.91}]X_{0.81}O_{20}(OH)_4$; X = (OH,F, Cl) = 23.82 g/mol, the elemental mass fractions of the main elements are calculated. The same is done for the admixture with the synthetic Zn-montmorillonite. These values are used to calculate colloid concentrations based on the ICP-MS data under the assumption that the total Zn and Al concentration is colloid bound and originating from the bentonite rings. Maximum colloid concentrations of 1.4 mg/L and 1.7 mg/L

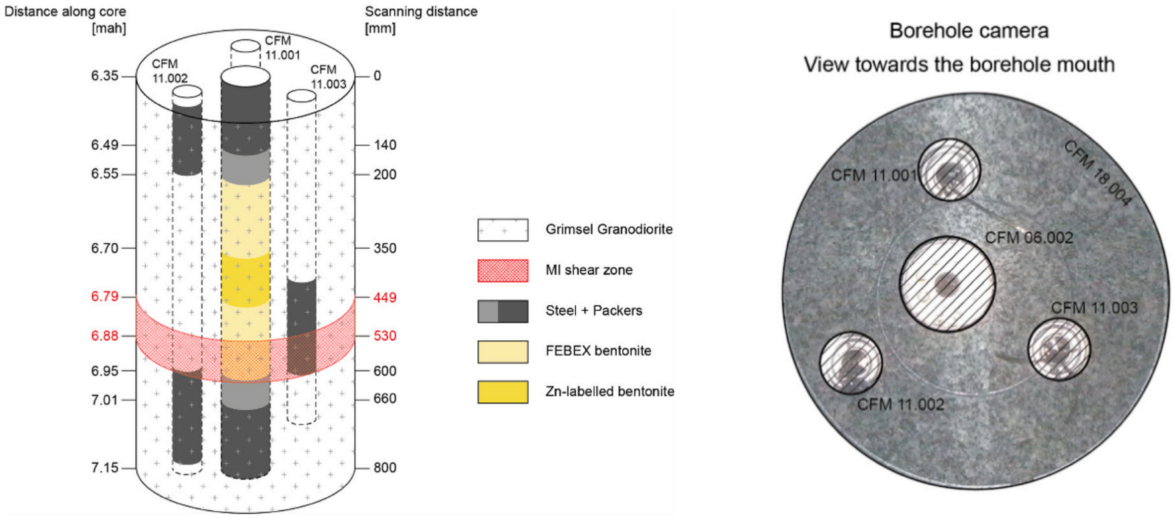

(a)

(b)

Fig. 1. a) Schematic of the cored interval with the position of the four boreholes, the packers, the bentonite source, and the envelope of the shear zone (i.e., the target fault). b) View directions toward the borehole end.

(Rinderknecht, 2017) are calculated from the zinc and aluminum concentrations, respectively (Huber et al., 2014).

2.5. Drilling procedure/dismantling

The experiment was over-cored (0-6 m drilled in 360 mm, coring from 6 to 7.7 m with 300 mm; core length was 1.7 m and 300 mm diameter) before cutting down for the CT analysis of the central part (core length 800 mm, at 6.35 to 7.15 m from tunnel surface) and after these CT measurements sliced into discs for various further analyses. Each section included, from the inside out, the steel mandrill, the bentonite ring, and the surrounding rock. The drilled core included a transversal section of the central source borehole (CFM 06.002) inside the steel and sections of the three near-field monitoring boreholes (CFM 11.001, CFM 11.002, and CFM 11.003) inside the rock area. Some cables and linings remained in the monitoring areas.

2.6. CT scanning and DRP workflow

The procedure involved multiple stages to ensure high-quality imaging. First, the over-cored 800 mm long sample was carefully stabilized to minimize movement and prevent material displacement during transport. The sample was then secured within a specialized scanning chamber, where it underwent rotational imaging by a fan-beam CT scanner at multiple angles. The scans were performed at EMPA (Swiss Federal Laboratories for Materials Science and Technology). The top and bottom section of the core was scanned at 5 mm intervals (i.e., scan spacing along core), while the central location over the traced bentonite and the shear fault zone was scanned at 0.50 mm resolution. Only this higher resolution data was used in this study. Each cross-sectional image has a resolution of 0.39 mm. This final image has a size of 1800 × 1800 × 400 voxels^3, which is equal to 708.3 × 708.3 × 200 mm^3.

Slight beam hardening artifacts, (bright rims and grayscale gradients toward the core centre) were observed in the CT images. In this study, no post-processing correction for beam hardening was applied. However, its potential influence on segmentation and intensity-based erosion estimates is acknowledged. Since the analysis focused on relative changes and spatial patterns, particularly in regions adjacent to the shear zone, rather than absolute grayscale values across the entire core, the impact of beam hardening on the main findings is expected to be limited.

The workflow for the DRP analysis is illustrated in Fig. 2. This process involved creating a digital twin model of the borehole system from the CT scan images. The scanned images first underwent a preprocessing step, which is crucial for enhancing the quality and usability of the scans for further analysis. A non-local K-mean filter (Buades et al., 2011) was then applied, known for its effectiveness in preserving edge information while reducing noise.

2.7. Segmentation using RF

Given the scans' composition of diverse materials such as compacted bentonite, rock matrix, open fracture, fault gouge, and steel mandrill, segmentation represents a complex challenge. Therefore, a segmentation method employing a RF classifier (Breiman, 2001) was applied, which uses multiple decision trees and has been previously shown to improve segmentation compared to simple thresholding methods. The segmentation accuracy was further enhanced by carefully selecting the Region of Interest (RoI), to limit interference from non-relevant areas, focusing the analysis on zones relevant to the research objectives.

The RF algorithm (Fig. 3) is a ML technique that classifies pixels by constructing multiple decision trees and aggregating their outputs (also called bagging) (Geurts et al., 2009; Reinhardt et al., 2022). This ensemble-based approach is commonly used to improve robustness and reduce overfitting in image segmentation tasks (i.e., poor generalization on unseen data) (Breiman, 2001; Cardenas-Gallegos et al., 2025; Sharr et al., 2024), and is suitable for segmenting complex multiphase images. Multiple decision trees (here 100 trees) are built using random subsets of both the data and features, which helps introduce variability among the trees, reducing the risk of overfitting.

In the segmentation task, the RF algorithm operates by analysing the spatial and contextual relationships between pixels. Various image features, such as pixel intensity, texture, and edges, are used as input parameters for the classification task (Sommer et al., 2011). Moreover, these features are derived by applying filters at different scales to the input images, typically using Gaussian filters with variable standard deviations (i.e., the scale parameter, σ) (Sommer et al., 2011). Each Gaussian filter acts on the image by suppressing high-frequency components, depending on the value of its standard deviation, and produces smoothed image outputs that can then be used to derive features (Urazmatov et al., 2024). By adjusting the scale parameter, one can control the filter's sensitivity to structures of varying sizes, enabling a more comprehensive analysis during the training phase.

In this study several filter types were implemented for each feature category (Table 1). For example, the Gaussian blur filter, applied at multiple kernel sizes, was used to generate features related to pixel intensity. Additionally, the Laplacian of Gaussian (LoG), Gaussian Gradient Magnitude (GGM), and difference of Gaussians (DoG) filters were applied to extract edge-related features that capture boundaries between different phases. The LoG filter (also referred as Marr-Hildreth operator) highlights regions with rapid intensity changes, effectively detecting edges (Jäger and Jutzi, 2023), GGM computes the gradient of an image by calculating Gaussian derivatives, aiding in identifying areas of significant intensity variation (Sanders et al., 2016), and the DoG filter emphasizes features at specific scales by subtracting one Gaussian-blurred image from another with a different scale parameter (Sandić-Stanković et al., 2022; Sommer et al., 2011). Lastly, Structure Tensor Eigenvalues (TE) and Hessian of Gaussian (HoG) Eigenvalues were used to evaluate the predominant directions of intensity variations (Arganda-Carreras et al., 2017; Sertcelik and Kafadar, 2012; Sommer et al., 2011), assisting in the detection of oriented structures and textures inside of target images. In this study, Gaussian filters with seven standard deviations (0.3, 0.7, 1.0, 1.6, 3.5, 5.0, and 10.0) for pixel intensity features

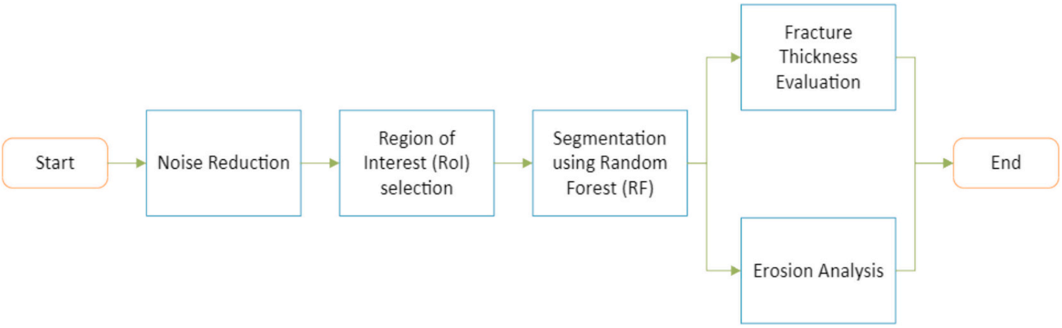

Fig. 2. Flowchart of digital rock physics workflow.

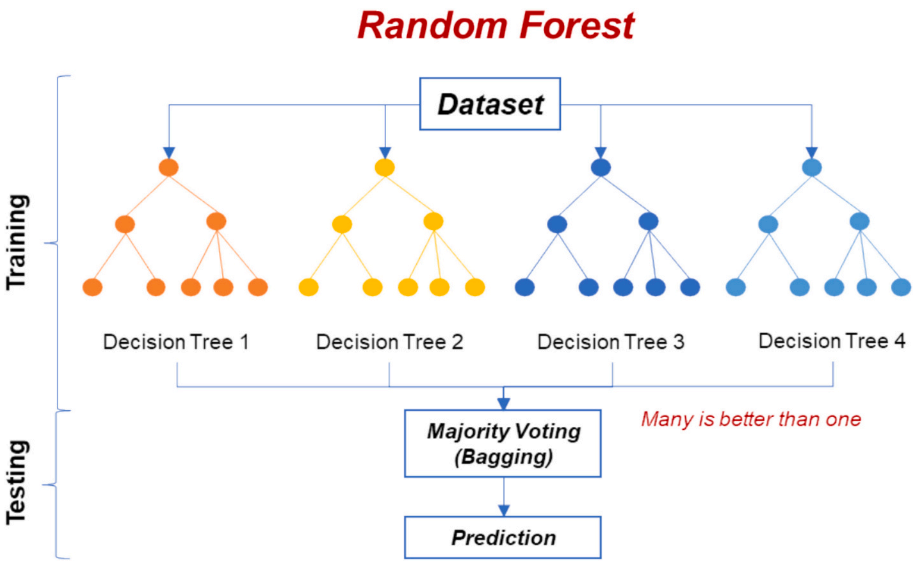

Fig. 3. Random Forest algorithm used for segmentation.

Table 1
Examples of filters used to extract image features.

Feature Category	Filter	Description
Intensity	Gaussian Smoothing	Applies a Gaussian filter to reduce noise.
Edge	Laplacian of Gaussian	Highlights regions of rapid intensity change by applying a Laplacian filter to the Gaussian-smoothed image.
	Gaussian Gradient Magnitude	Measures the rate of intensity change in the image.
	Difference of Gaussians	Emphasizes features at specific scales by subtracting one Gaussian-blurred image from another.
Texture	Structure Tensor Eigenvalues	Evaluates the predominant directions of intensity variations, aiding in the detection of oriented structures and textures.
	Hessian of Gaussian Eigenvalues	Applies the Gaussian filter followed by second-order partial derivatives of the image, which provides information about the local curvature of images.

were used, while six standard deviations (0.7, 1.0, 1.6, 3.5, 5.0, and 10.0) were used for the other filters (LoG, GGM, DoG, TE, and HoG), resulting in a 37-feature vector for each pixel (See Table 2)

Those 37 features were generated by systematically applying a set of commonly used image filters across multiple spatial scales. The filters were selected based on prior studies showing their relevance in capturing intensity, edge, and texture information in multi-phase systems (Arganda-Carreras et al., 2017; Sommer et al., 2011). The objective was to retain a comprehensive feature set that captures relevant structures at different scales. However, feature importance evaluation using Random Forest could be considered in future work to reduce dimensionality and improve model efficiency.

All image processing tasks were carried out in Dragonfly Pro (Object Research Systems Inc., Version 2021). For RF segmentation, the *ilastik* segmentation toolkit (Berg et al., 2019) was employed. Upon successful segmentation, detailed analyses such as the determination of fracture aperture distribution and quantification of bentonite erosion were conducted. By integrating DRP workflows and image processing tools, this study aims to enhance the analysis of subsurface structures and their dynamic processes, building on established geological methods.

3. Results and discussion

3.1. RF segmentation

The CT scan images first underwent a denoising process using Non-Local Mean Filter (NLMF) (Buades et al., 2011), enhancing the clarity of bentonite rings and fracture networks (Fig. 4). Unlike traditional denoising methods (e.g., mean or median filters), which consider only a pixel and its surrounding neighbours, NLMF eliminates noise by comparing the similarity of patches across the entire image and weighting pixels based on their resemblance to the target pixel. This process prevents image blurring, a common issue in conventional smoothing filters.

During the segmentation, there are several phases that are not relevant to the analysis in the RoI, such as the central steel mandril and various linings within the internal structure of the sections of the four boreholes. These phases and objects exhibit similar greyscale intensities, making accurate segmentation challenging. The greyscale distribution of the CT image across various phases is displayed in Fig. 5a. While the bentonite rings and rock matrix have distinct greyscale values, there is significant overlap in the greyscale values of fault gouge and open fractures, making it difficult to separate these phases. Furthermore, the tools inside the main borehole (CFM 06.002) completely overlap with other phases and are distributed across nearly the entire greyscale range (i.e., 0 to 255). Therefore, careful selection of RoI during segmentation is crucial to improving accuracy and ensuring meaningful analysis.

Table 2
Details of calculations for bentonite ring erosion estimation from different scenarios.

Scenario	Description	Assumed Porosity (%)	Original partially eroded voxels	Fully eroded voxels	Equivalent eroded voxels	Erosion rate (kg/m^2/a)
1	All partially eroded voxels assumed to be fully eroded	100	41,789	3451	45,240	1.31
2	A porosity range was estimated for partially eroded voxels	72.7			33,831	0.99

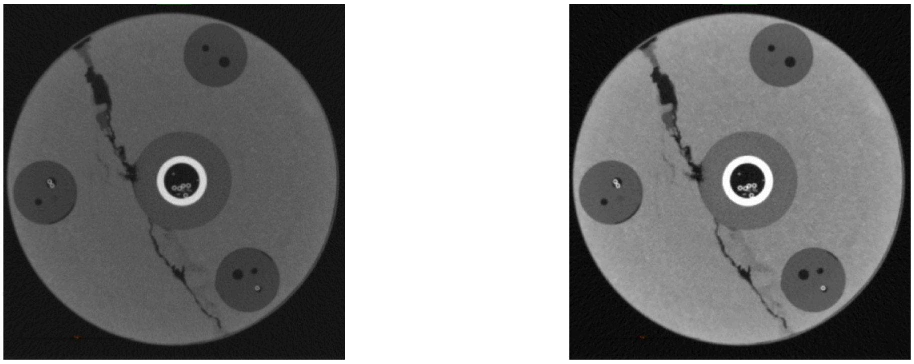

(a) (b)

Fig. 4. Comparing (a) the original CT scan with (b) the filtered scan by NLMF.

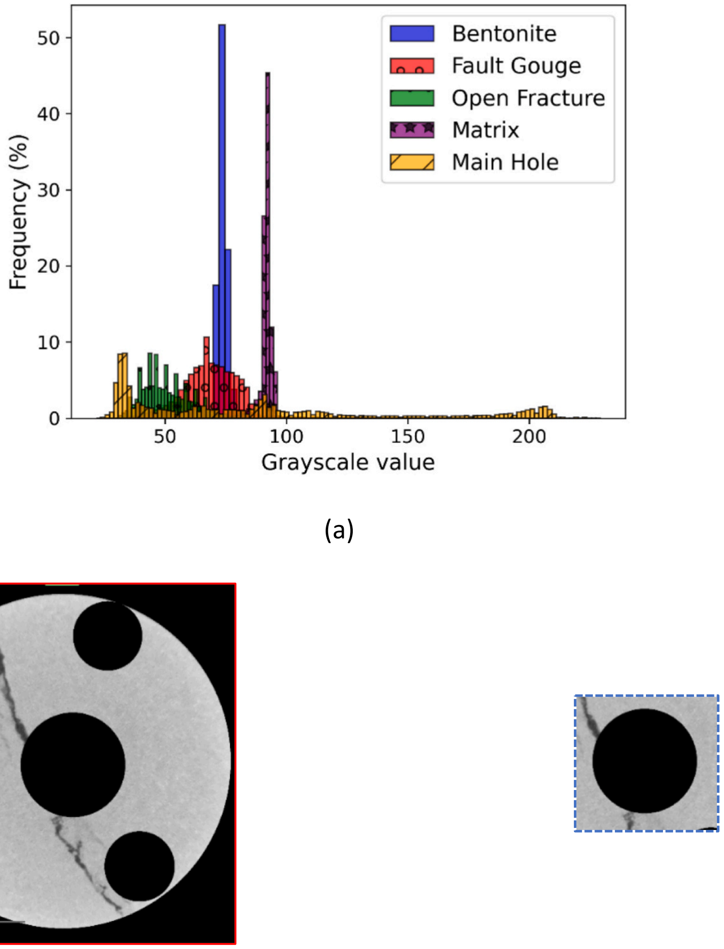

(a)

(b) (c)

Fig. 5. (a) Greyscale value for various phases available in the CT scan images. (b) RoI for fault thickness analysis (red solid frame). Masking of the four boreholes to reduce segmentation interferences from non-important areas. (c) Second RoI (blue dashed frame) for bentonite ring analysis. By main hole the central part of the packer is meant. (For interpretation of the references to colour in this figure legend, the reader is referred to the web version of this article.)

During the analysis, two main RoIs were selected. To evaluate the fault thickness, the background of the CT scan, as well as all four main holes, were removed from the RoI (Fig. 5b). For the bentonite mass loss analysis, only the area surrounding the central borehole (CFM 06.002) (including the fault area) was considered (Fig. 5c). In this RoI, the materials inside the main borehole were masked out to reduce irrelevant information.

Various filters were applied to extract relevant features during RF training in this study, with Gaussian blur used to capture pixel intensity variations and more advanced filters such as LoG, GGM, and DoG used for edge detection. Additionally, TE and HoG helped identify textures. A 37-feature vector was generated per pixel, integrating these filters with different standard deviations. Fig. 6 provides a detailed visual comparison of the original image alongside the results of various filters at variable Gaussian smoothing standard deviations of 1, 3.5, and 10. It is shown how each filter type emphasizes different aspects of the input image, demonstrating the contributions of each feature to the overall segmentation performance.

The digital twin achieved after segmentation by the RF algorithm is shown in Fig. 7, highlighting its effectiveness in identifying distinct phases, including steel mandrill, bentonite rings, fault gouge, open fractures and the rock matrix (which is not shown in this figure). The segmentation process reveals clear distinctions between different material phases. The results demonstrate that applying multiphase segmentation in combination with carefully selected RoIs enables accurate and reliable image analysis, facilitating a more detailed evaluation of the

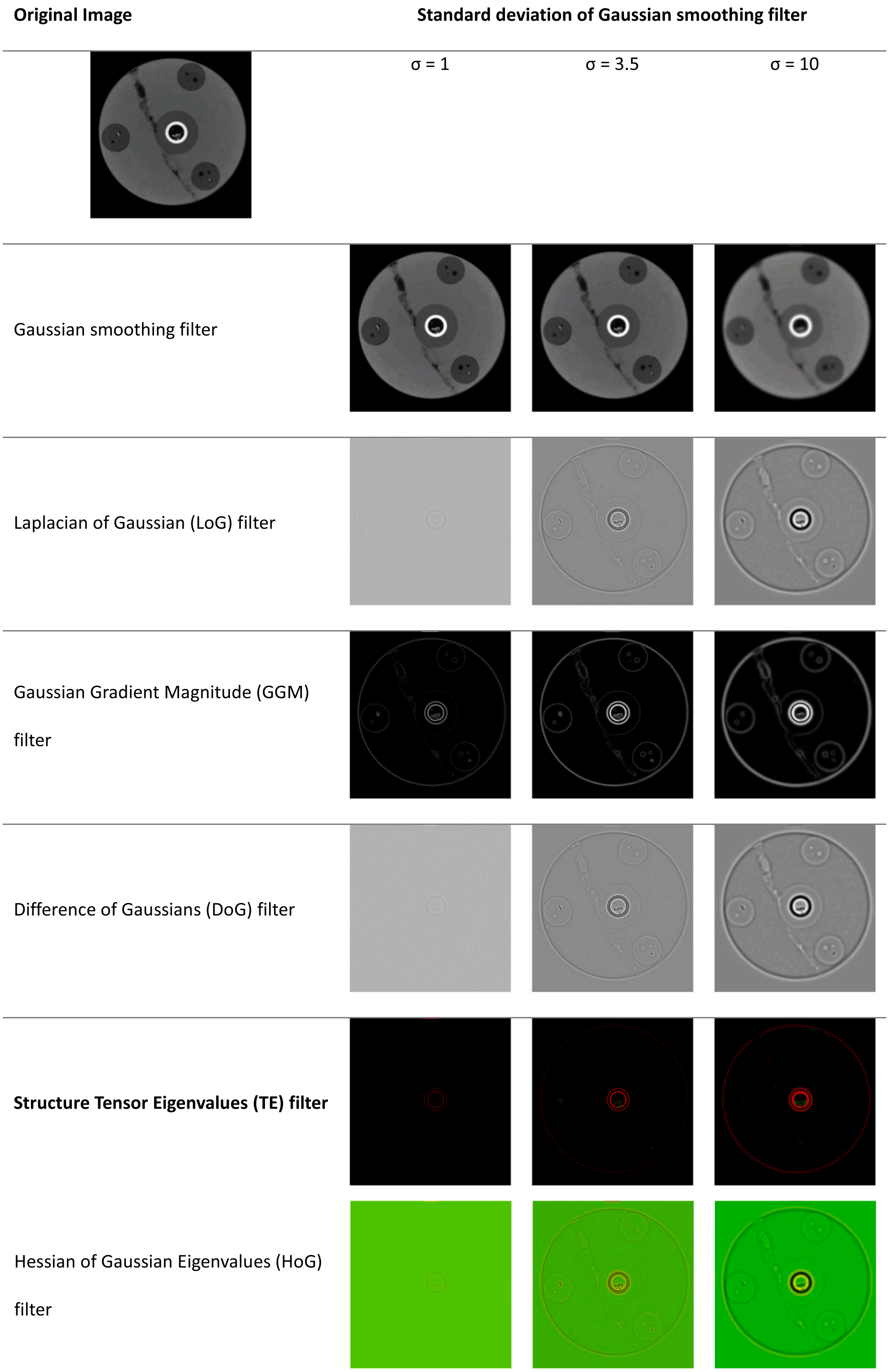

Fig. 6. Representation of features extracted from top view of the main borehole. From left to right: three various Gaussian smoothing with a standard deviation of 1, 3.5, and 10. From top to bottom: various applied filters.

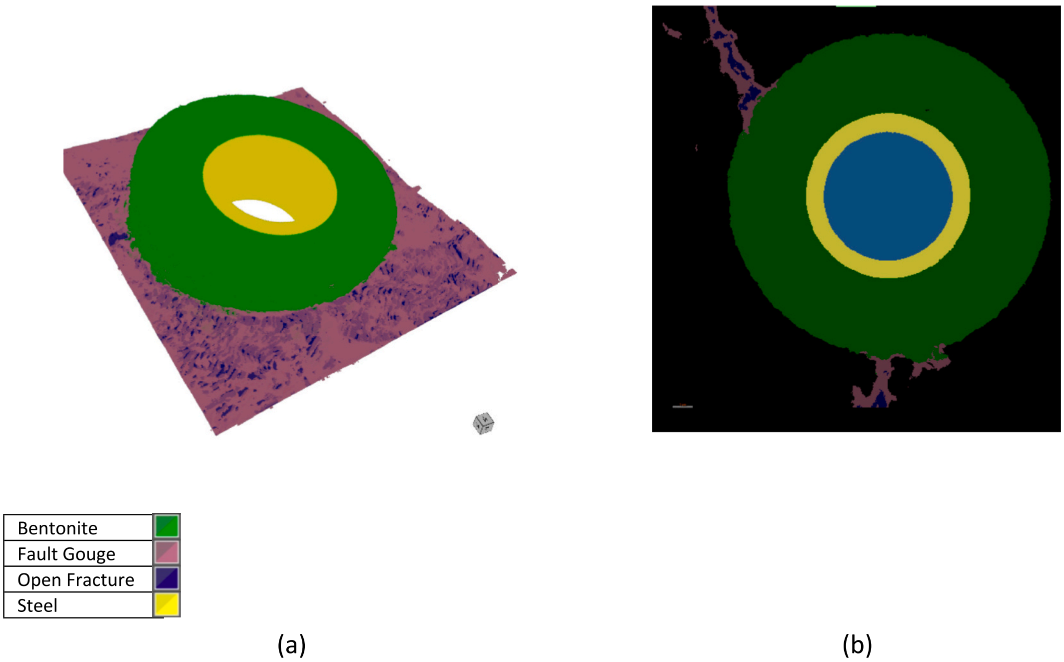

Fig. 7. (a) 3D and (b) 2D segmentation results using the RF algorithm. In the 2D image, the black background is the host rock.

geological features under investigation.

3.2. Fault aperture analysis

The fault aperture and topology within the shear zone were analysed to better understand its structural and geometrical characteristics and contact area to the compacted bentonite. A 3D fault thickness map is depicted in Fig. 8a, highlighting the spatial distribution of the fault volume connecting the central borehole (CFM 06.002) to the three neighbouring monitoring boreholes (CFM 11.001, CFM 11.002, and CFM 11.003).

The fault has an aperture ranging from 0.85 to 6.93 mm with a mean (2σ) of 2.90 ± 1.09 mm (Fig. 8b). The surface to volume ratio of the fault is 1.067. The variability in fault thickness underscores the geometric complexity of the shear zone and highlights the care to be taken abstracting fault geometry toward parallel plate models (Stoll et al., 2019). Comparable results have been found in the EP (Excavation Project) impregnating the fracture network with fluorescent resin and subsequently over-coring along the shear zone and cutting into slices of ~3-cm thickness (Frieg et al., 1998). The surfaces of these slices were then photographed in visible and ultraviolet (UV) light to obtain an aperture distribution varying from a low-end cut-off of 10 μm (below the CT resolution) to an upper-end cut-off of 2 cm (Mettier et al., 2006).

Finally, the fracture aperture distributions between the main borehole and each of the three monitoring boreholes sections were evaluated. To do so, a crop from the fault region between the central borehole and each neighbouring borehole (shown in Fig. 8a with three boxes of variable colors) was considered. For each crop, the fault thickness map was evaluated. The fracture aperture distribution between the central borehole and the three monitoring boreholes is shown in Fig. 8c. The analysis reveals significant variations in fracture apertures, which are likely to affect the flow dynamics and the stability of the engineered barrier system over time. For example, the dipole connecting the main hole to CFM11.001, CFM11.002, and CFM11.003 has a mean fault thickness of 2.26 ± 0.86 mm, 2.99 ± 0.91 mm, and 2.69 ± 0.99 mm, respectively. The lower fracture aperture between CFM 11.001 and CFM 06.002 supports the findings from hydraulic testing, where the hydraulic connection between these two boreholes was found to be lower (Lanyon et al., 2014).

3.3. Bentonite erosion evaluation and its uncertainty

Once the bentonite rings come into contact with groundwater, the bentonite will swell into any open porosity, including the small annular gap between the rings and the borehole walls because of the additionally constructed cover sleeve, and any open fracture voids at the borehole wall. After calibration, the average swollen diameter of 86.9 mm was computed by measuring different locations of altered bentonite rings in the CT scan images, far from the fault region. This value was then used to update the bentonite ring density.

The FEBEX bentonite rings, during manufacturing and before installation into the main borehole, had a ring diameter of 82 mm with a dry density of 1.65 ± 0.01 Mg/m^3 and the nominal emplaced diameter of the borehole was 86.00 mm. The rings had a 13.9 % gravimetric water content. Since all 12 FEBEX rings were precisely weighed before installation and given their new final swollen diameter measured from CT data (86.87 mm), the final average density of the bentonite rings was evaluated to be 1.31 Mg/m^3. This average value was considered for each voxel to compute the erosion weight during 4.5 years of the LIT.

To quantify erosion, a cylindrical mask was applied around the target FEBEX bentonite rings, allowing for the analysis of material loss. The scan was then segmented into four phases of intact bentonite, partially eroded voxels, fully eroded voxels (with 100 % porosity), and steel mandrill (Fig. 9). As it is indicated in Fig. 9, the distribution of voxels identified as eroded, clearly showing their concentration in proximity to the shear zone. The spatial clustering supports the interpretation that erosion is localized and likely driven by shear-induced processes, rather than random noise or imaging artifacts. By counting the segmented eroded volume from the initial structure within the cylindrical bentonite mask, the extent of erosion was quantified. This approach enabled precise calculations of bentonite mass loss and helped in comparing CT-based erosion estimates with independent geochemical assessments, such as the colloid quantification by means of LIBD/ICP-MS.

The multiphase segmentation using the RF algorithm was applied slice by slice on 2D image data; however, since these slices are part of a registered 3D volume, the segmented pixels correspond to voxels in three-dimensional space. Out of 9,900,000 voxels in the RoI, a total of 3451 fully eroded voxels and 41,789 partially eroded voxels were identified, each voxel having a size of 0.39 × 0.39 × 0.5 μm (7.72 ×

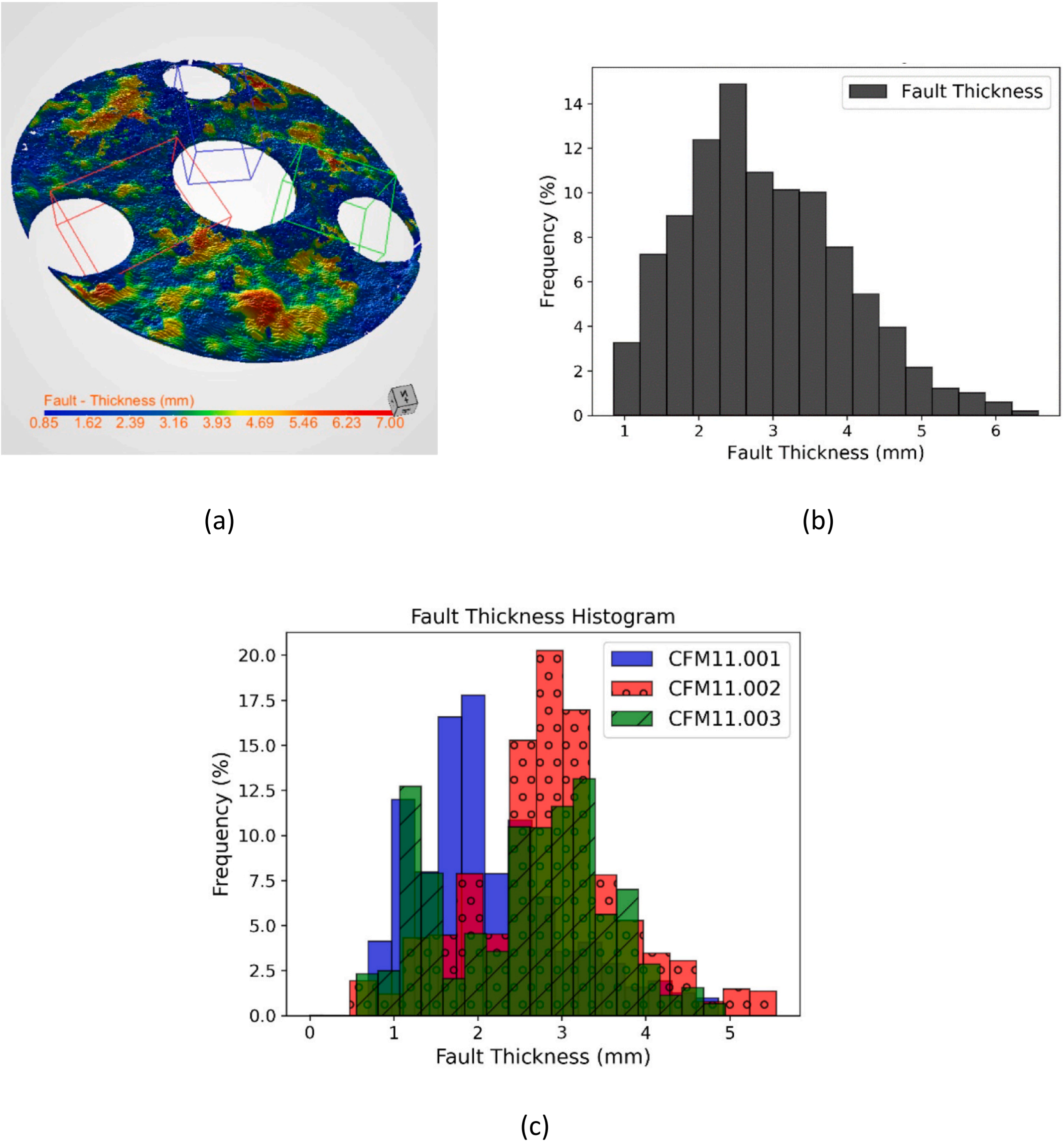

Fig. 8. (a) 3D Fault thickness map. The fault volume connecting neighbouring boreholes to the central borehole is also highlighted by three boxes in different colors (b) Fault thickness histogram. (c) Dipole aperture distributions between the main borehole (CFM 06.002) and the three neighbouring monitoring holes (CFM 11.001, CFM 11.002, and CFM 11.003) as indicated by the coloured boxes.

10^{-11} m^3). These values represent a small but spatially localized fraction of voxels, predominantly concentrated near the shear zone (see Fig. 9). While the overall proportion is low, the non-random distribution supports the interpretation that the grayscale variations are due to localized erosion rather than imaging artifacts or material inhomogeneities.

A 100 % porosity was considered for the fully eroded voxels. These voxels based on their dark greyscale value were easily differentiated from the other voxels during the segmentation using RF. However, those voxels that have higher grey intensity were separated from these voxels and assigned as partially eroded voxels. In othe+r words, just a fraction of the bentonite was eroded in these voxels during the 4.5-year LIT experiments. To estimate the uncertainty of erosion, two scenarios were considered. In the pessimistic case all these voxels were considered as fully eroded, which is the maximum possible erosion. In a more realistic scenario, the porosity of these voxels is estimated based on their greyscale range in comparison to the greyscale value of unaltered bentonite rings.

The histogram of greyscale intensity value of bentonite rings and partially eroded voxels are depicted in Fig. 10, which span in a greyscale range of 0 to 145 (with a mean of 74) and 0 to 79 (mean of 33) out of 255, respectively. Since no calibration data of density versus greyscale intensity was available, it was decided to roughly estimate the porosity of the eroded voxels using the unaltered bentonite ring area in the CT images. It is assumed that the porosity of the internal bentonite voxels (i.e., those far from the erosion surface) remain constant over time and are equal to the initial porosity of 38.9 % (Schlickenrieder et al., 2017). As the resolution of CT scanning was not high enough to resolve the microporosity within the bentonite rings; therefore, the mean greyscale intensity ($G_{b,2} = 74$) in the bentonite greyscale histogram is assumed of this porosity value (38.9 %). Consequently, the other tail of this histogram ($G_{b,1} = 0$) given by the partially eroded voxels of the same material represents approximately 100 % porosity (i.e., a pore voxel). If the partially eroded voxels follow a linear trend between greyscale intensity and porosity, like unaltered bentonite rings, then using Eq. (1) the mean intensity range of partially eroded voxels (33 out of 255) corresponds to the porosity of approximately 72.7 %, which shows that these voxels have 33.8 % higher porosity than unaltered bentonite voxels (38.9 %).

$$\Phi_{pe} = \left(G_{pe} - G_{b,1}\right)\frac{\Phi_{b,1} - \Phi_{b,2}}{G_{b,2} - G_{b,1}} + \Phi_{b,2} \tag{1}$$

Fig. 9. **a)** 3D segmentation results using the RF algorithm for erosion evaluation. A cylindrical mask was applied around the FEBEX rings. b) The same as (a) but the bentonite voxels were not shown for comparison purpose.

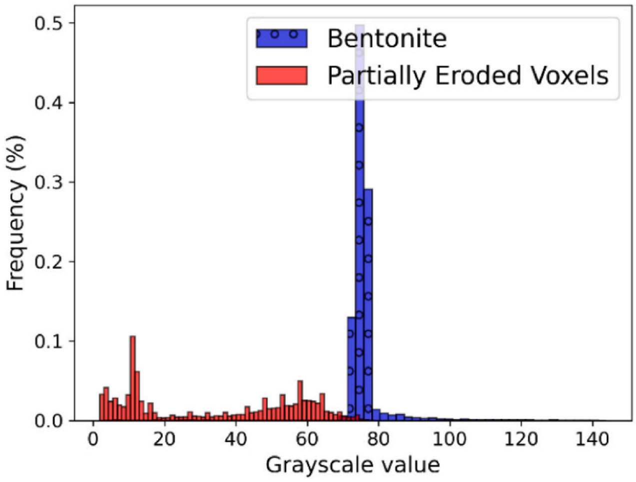

Fig. 10. Grey intensity histogram for bentonite and partially eroded voxels.

It is important to acknowledge that the estimation of bentonite mass loss based solely on CT grayscale intensity data, without a supporting calibration data relating grayscale values to material density, might introduce uncertainties in the quantitative analysis. Although this assumption may not be completely correct, at least it provides a rough estimate of eroded voxel porosity. Consequently, the quantitative erosion values presented should be regarded as indicative rather than definitive, serving primarily to highlight relative trends rather than absolute mass loss. However, the pessimistic scenario, in which all partially eroded voxels are considered fully eroded, represents the maximum possible mass loss. This approach provides an upper bound estimate of bentonite erosion, serving as a conservative reference that likely overestimates the actual erosion but offers a useful limit for interpretation. By comparing this maximum erosion estimate with the more conservative, grayscale-based calculation, we gain a better understanding of the potential range of bentonite loss, thereby framing the uncertainty and improving the overall assessment.

The following table summarizes the eroded amount for different scenarios. In the scenario, where all partially eroded voxels are assumed to be fully eroded (i.e., pessimistic assumption), the total number of eroded voxels is 45,240. Given the voxel volume of 7.72×10^{-11} m^3 and the corrected bentonite density of 1.31 Mg/m^3, the total bentonite erosion over 4.5 years (1600 days) of the LIT is estimated to be 1.04 g/y. In the second scenario, where the mean porosity of partially eroded voxels is accounted for, the estimated erosion rate would be 0.78 g/y. By considering the mean fault aperture (2.90 ± 1.09 mm) and the given bentonite diameter of 86.87 mm, a contact area between fault and bentonite rings of $7.91{\cdot}10^{-4}$ m^2 can be estimated. Thus, the contact area normalized erosion rates will be between 0.99 and 1.31 $kg/m^2/y$. The erosion percentage toward the three neighbouring boreholes (CFM11.001, CFM11.002, and CFM11.003) was estimated to be 21 %, 45 %, and 34 %, respectively, which is in accordance with the average fault contact areas of $6.16{\cdot}10^{-4}$ m^2, $8.16{\cdot}10^{-4}$ m^2, and $7.34{\cdot}10^{-4}$ m^2. The findings indicate that the maximum erosion occurred in the direction from the central borehole toward CFM11.002, which has the highest average fault thickness (2.99 ± 0.91 mm) as well as contact area.

Water samples from near-field borehole intervals in CFM11.001, CFM11.002, and CFM11.003 showed estimated colloid concentrations of 1.4–1.7 mg/L back-calculated based on the element mass fractions in the FEBEX bentonite structural formula. These values are calculated under the assumption that the total Zn or Al concentration is colloid bound and originating from the bentonite rings, respectively. LIBD measurements in the same boreholes revealed approx. 0.07 mg/L colloidal concentrations. Further analysis of the “Pinkel” surface packer showed mean concentrations of 0.005 mg/L nanoparticulate fraction. Taking an extraction flow of 0.05 mL/min at the observation boreholes CFM11.001, CFM11.002, and CFM11.003 and 25 mL/min at the Pinkel surface packer a mass loss rate of 0.001 g/y (LIBD), 0.045 g/y (ICP-MS) and 0.066 g/y (for Pinkel) could be estimated, which results in contact area normalized erosion rates of 0.002 to 0.107 $kg/m^2/y$. The significantly lower erosion rates quantified via groundwater monitoring analysis can be explained by the colloid retardation observed even under these unfavorable colloid attachment conditions in migration studies (Reiche et al., 2016).

Most importantly, all estimated erosion values, including the pessimistic scenario, remain below the critical range for repository evaluation regarding mass loss, reinforcing the long-term integrity of FEBEX bentonite as a geotechnical barrier material. A buffer failure criterion set by SKB is a mass loss of 1200 kg from originally 22,000 kg in one emplacement hole (SKB, 2011). Both techniques used in this study show erosion rates <2 $kg/m^2/y$, at least two orders of magnitude below mass loss assessment rates of 500 to 1500 $kg/m^2/y$ (POSIVA, 2017).

4. Conclusion

This study investigated the impact of a fractured zone on bentonite erosion in an in-situ experiment at the Grimsel Test Site (GTS), Switzerland, simulating a bentonite barrier in a deep geological repository for radioactive waste. By combining X-ray computed tomography scanning, digital rock physics, and segmentation with a Random Forest classifier in ilastik applied to the over-cored sample, we obtained a detailed quantification of the distribution of fault apertures and bentonite loss. The correct selection of the region of interest played a crucial role in minimizing segmentation errors, while uncertainty analysis refined erosion estimates.

The results demonstrate that the fault aperture distribution within the shear zone is highly heterogeneous, with a mean aperture of 2.90 ± 1.09 mm. This variability in fault thickness controls hydrodynamics in the fracture and underscores the complexity of fluid and particle transport within the shear zone. Further, careful consideration is advocated when using abstracted fault geometries to assess the long-term performance of engineered barrier systems in geological repositories. Hydraulic characterization between the central and the monitoring boreholes confirmed heterogeneity not only in the fracture aperture but also in the hydraulic connectivity.

The random forest segmentation approach enabled a clear visual separation of different material phases, including bentonite, rock matrix, fault gouge, and open fractures, based on their distinct greyscale and textural features in the CT images. This method improved the accuracy of mass loss quantification and fault characterization, overcoming the limitations of traditional thresholding techniques. Although not benchmarked against other segmentation methods, the benefit of this approach was validated qualitatively through expert visual inspection and its ability to support robust, consistent phase distinction essential for downstream analysis.

The segmentation results revealed that the bentonite rings experienced partial and heterogenous erosion, with the total erosion rate estimated to be between 0.99 and 1.31 $kg/m^2/y$ for FEBEX bentonite. All estimated erosion values remain below the critical range for repository evaluation regarding mass loss, reinforcing the long-term integrity of FEBEX bentonite as a geotechnical barrier material within the tested conditions. The erosion rates estimated within this study are <2 $kg/m^2/a$ and therefore at least two orders of magnitude below mass loss assessment rates of 500 to 1500 $kg/m^2/a$ (POSIVA, 2017). The erosion masses within this study was FEBEX bentonite a Ca—Mg dominated bentonite. Based on colloid migration studies performed so far, which show lower colloid recovery compared to the conservative tracer in this shear zone (Reiche et al., 2016), it is assumed that the significantly lower erosion rates estimated via groundwater monitoring analysis can be linked to colloid retardation/attachment to fracture surfaces or clogging.

CRediT authorship contribution statement

Saeid Sadeghnejad: Writing – review & editing, Writing – original draft, Visualization, Validation, Software, Methodology. **Sarah Hupfer:** Investigation. **Janis Pingel:** Investigation. **Bill Lanyon:** Writing – original draft, Methodology, Conceptualization. **Raphael Schneeberger:** Writing – original draft, Project administration, Conceptualization. **Ingo Blechschmidt:** Project administration, Conceptualization. **Ursula Alonso:** Writing – original draft, Investigation, Conceptualization. **Wolfgang Hauser:** Validation, Investigation, Conceptualization. **Stephanie Kraft:** Investigation. **Horst Geckeis:** Project administration, Funding acquisition, Conceptualization. **Thorsten Schäfer:** Writing – review & editing, Writing – original draft, Project administration, Investigation, Funding acquisition, Conceptualization.

Declaration of competing interest

The authors declare that they have no known competing financial interests or personal relationships that could have appeared to influence the work reported in this paper.

Acknowledgement

This work is financed by the Federal Ministry for the Environment, Nature Conservation, Nuclear Safety and Consumer Protection (BMUV) under Contract 02E12153A-C (Project “EVIDENT”). We also would like to thank the other partners of the CFM project at Grimsel Test Site: currently, BGE (Germany), Kaeri (Republic of Korea), NUMO (Japan), NWS (UK), and Nagra (Switzerland). The authors acknowledge the assistance of ChatGPT-3.5 (developed by OpenAI) for proofreading support. The final content and interpretations are solely the responsibility of the authors.

Data availability

Data will be made available on request.

References

Alexander, W.R., Ota, K., Frieg, B., 2001. The NAGRA-JNC In Situ Study of Safety Relevant Radionuclide Retardation in Fractured Crystalline Rock II: The RRP Project Methodology Development, Field and Laboratory Tests. NAGRA, Wettingen, Switzerland.

Arganda-Carreras, I., Kaynig, V., Rueden, C., Eliceiri, K.W., Schindelin, J., Cardona, A., Sebastian Seung, H., 2017. Trainable Weka segmentation: a machine learning tool for microscopy pixel classification. Bioinformatics 33, 2424–2426.

Berg, S., Kutra, D., Kroeger, T., Straehle, C.N., Kausler, B.X., Haubold, C., Schiegg, M., Ales, J., Beier, T., Rudy, M., 2019. Ilastik: interactive machine learning for (bio) image analysis. Nat. Methods 16, 1226–1232.

Birgersson, M., Hedström, M., Karnland, O., 2011. Sol formation ability of ca/Na-montmorillonite at low ionic strength. Phys. Chem. Earth Parts A/B/C 36, 1572–1579.

Bossart, P., Mazurek, M., 1991. Grimsel Test Site: Structural Geology and Water Flow-Paths in the Migration Shear Zone. Nagra Technical Report NTB 91-12. Nagra, Wettingen, Switzerland.

Breiman, L., 2001. Random forests. Mach. Learn. 45, 5–32.

Buades, A., Coll, B., Morel, J.-M., 2011. Non-local means denoising. Image Process. On Line 1, 208–212.

Cardenas-Gallegos, J.S., Severns, P.M., Klimeš, P., Lacerda, L.N., Peduzzi, A., Ferrarezi, R.S., 2025. Reliable plant segmentation under variable greenhouse illumination conditions. Comput. Electron. Agric. 229, 109711.

Cuadros, J., Linares, J., 1996. Experimental kinetic study of the smectite-to-illite transformation. Geochim. Cosmochim. Acta 60, 439–453.

Delavernhe, L., Steudel, A., Darbha, G.K., Schäfer, T., Schuhmann, R., Wöll, C., Geckeis, H., Emmerich, K., 2015. Influence of mineralogical and morphological properties on the cation exchange behavior of dioctahedral smectites. Colloids Surf. A Physicochem. Eng. Asp. 481, 591–599.

Dhanachandra, N., Manglem, K., Chanu, Y.J., 2015. Image segmentation using K-means clustering algorithm and subtractive clustering algorithm. Proc. Comput. Sci. 54, 764–771.

Friedrich, F., Schild, D., Weidler, P., Schäfer, T., 2016. Hydration of FEBEX bentonite observed by environmental scanning electron microscopy (ESEM). Clay Miner. Soc. Worksh. Lect. Ser. 21, 199–210.

Frieg, B., Alexander, W.R., Dollinger, H., Bühler, C., Haag, P., Möri, A., Ota, K., 1998. In situ resin impregnation for investigating radionuclide retardation in fractured repository host rocks. J. Contam. Hydrol. 35, 115–130.

García-Romero, E., María Manchado, E., Suárez, M., García-Rivas, J., 2019. Spanish bentonites: a review and new data on their geology, mineralogy, and crystal chemistry. Minerals 9, 696.

Geckeis, H., Schäfer, T., Hauser, W., Rabung, T., Missana, T., Degueldre, C., Möri, A., Eikenberg, J., Fierz, T., Alexander, W.R., 2004. Results of the colloid and radionuclide retention experiment (CRR) at the Grimsel Test Site (GTS), Switzerland -Impact of reaction kinetics and speciation on radionuclide migration. Radiochim. Acta 92, 765–774.

Gens, A., Sánchez, M., Guimarães, L.D.N., Alonso, E.E., Lloret, A., Olivella, S., Villar, M. V., Huertas, F., 2009. A full-scale in situ heating test for high-level nuclear waste disposal: observations, analysis and interpretation. Géotechnique 59, 377–399.

Geurts, P., Irrthum, A., Wehenkel, L., 2009. Supervised learning with decision tree-based methods in computational and systems biology. Mol. BioSyst. 5, 1593–1605.

Hauser, W., Geckeis, H., Kim, J.I., Fierz, T., 2002. A mobile laser-induced breakdown detection system and its application for the in situ-monitoring of colloid migration. Colloids Surf. A Physicochem. Eng. Asp. 203, 37–45.

Hu, G., Pfingsten, W., 2023. Data-driven machine learning for disposal of high-level nuclear waste: a review. Ann. Nucl. Energy 180, 109452.

Hu, M., Rutqvist, J., Steefel, C.I., 2021. Mesh generation and optimization from digital rock fractures based on neural style transfer. J. Rock Mech. Geotech. Eng. 13, 912–919.

Huang, C., Zhang, X., Liu, S., Li, N., Kang, J., Xiong, G., 2021. Construction of pore structure and lithology of digital rock physics based on laboratory experiments. J. Pet. Explor. Prod. Technol. 11, 2113–2125.

Huber, F., Noseck, U., Schäfer, T., 2014. Colloid/Nanoparticle Formation and Mobility in the Context of Deep Geological Nuclear Waste Disposal. Project KOLLORADO-2 Final report. KIT Scientific Report 7645. KIT Scientific Publishing, Karlsruhe.

Huber, F.M., Leone, D., Trumm, M., Moreno, L.R., Neretnieks, I., Wenka, A., Schäfer, T., 2021. Impact of rock fracture geometry on geotechnical barrier integrity – a numerical study. Int. J. Rock Mech. Min. Sci. 142, 104742.

Jäger, M., Jutzi, B., 2023. 3d density-gradient based edge detection on neural radiance fields (nerfs) for geometric reconstruction. arXiv preprint. arXiv:2309.14800.

Kapur, J.N., Sahoo, P.K., Wong, A.K., 1985. A new method for gray-level picture thresholding using the entropy of the histogram. Comput. Vision Graph. Image Process. 29, 273–285.

Karnland, O., Sandén, T., Johannesson, L.-E., Eriksen, T.E., Jansson, M., Wold, S., Pedersen, K., Motamedi, M., Rosborg, B., 2000. Long Term Test of Buffer Material. Final Report on the Pilot Parcels. SKB Tech. Rep. TR-00-22.

Kretzschmar, R., Schäfer, T., 2005. Metal retention and transport on colloidal particles in the environment. Elements 1, 205–210.

Lanyon, G.W., Blechschmidt, I., Schäfer, T., Kontar, K., Steiner, P., Martin, A.J., 2014. Generation of Bentonite Colloids Under Repository-Relevant Conditions in the CFM Long-Term in Situ Test. Grimsel Test Site, Switzerland, AGU Fall Meeting Abstracts, pp. H21B–0735.

Lee, S., Lee, C., 2010. Unsupervised segmentation for hyperspectral images using mean shift segmentation, satellite data compression, communications, and processing VI. SPIE 271–276.

Liu, L., Moreno, L., Neretnieks, I., 2009. A dynamic force balance model for colloidal expansion and its DLVO-based application. Langmuir 25, 679–687.

Lloret, A., Villar, M.V., 2007. Advances on the knowledge of the thermo-hydro-mechanical behaviour of heavily compacted "FEBEX" bentonite. Phys. Chem. Earth Parts A/B/C 32, 701–715.

Mettier, R., Kosakowski, G., Kolditz, O., 2006. Influence of small-scale heterogeneities on contaminant transport in fractured crystalline rock. Ground Water 44, 687–696.

Missana, T., Alonso, Ú., Turrero, M.J., 2003. Generation and stability of bentonite colloids at the bentonite/granite interface of a deep geological radioactive waste repository. J. Contam. Hydrol. 61, 17–31.

Möri, A., Alexander, W.R., Geckeis, H., Hauser, W., Schäfer, T., Eikenberg, J., Fierz, T., Degueldre, C., Missana, T., 2003. The colloid and radionuclide retardation experiment at the Grimsel Test Site: influence of bentonite colloids on radionuclide migration in a fractured rock. Colloids Surf. A Physicochem. Eng. Asp. 217, 33–47.

Moslemipour, A., Sadeghnejad, S., Enzmann, F., Khoozan, D., Hupfer, S., Schäfer, T., Kersten, M., 2025. Multi-scale pore network fusion and upscaling of microporosity using artificial neural network. Mar. Pet. Geol. 107349.

Niu, Y., Mostaghimi, P., Shabaninejad, M., Swietojanski, P., Armstrong, R.T., 2020. Digital rock segmentation for petrophysical analysis with reduced user bias using convolutional neural networks. Water Resour. Res. 56, e2019WR026597.

Noseck, U., Schäfer, T., Quinto, F., Bouby, M., Stoll, M., Huber, F., 2020. Integrity of the Bentonite Barrier for the Retention of Radionuclides in Crystalline Host Rock - Experiments and Modeling - (Project KOLLORADO-e2; Final Report); KIT Scientific Report 7757. KIT, Karlsruhe.

Otsu, N., 1979. A threshold selection method from gray-level histograms. IEEE Trans. Syst. Man Cybern. 9, 62–66.

POSIVA, 2017. KBS-3H System Design Phase 2011–2016: Final Report (Updated 2023–09), Posiva SKB Report 06. Svensk Kärnbränslehantering AB and Posiva Oy, Posiva Oy, Finland.

Quinto, F., Blechschmidt, I., Garcia Perez, C., Geckeis, H., Geyer, F., Golser, R., Huber, F., Lagos, M., Lanyon, B., Plaschke, M., Steier, P., Schäfer, T., 2017. Multiactinide analysis with accelerator mass spectrometry for ultratrace determination in small samples: application to an in situ radionuclide tracer test within the colloid formation and migration experiment at the Grimsel Test Site (Switzerland). Anal. Chem. 89, 7182–7189.

Quinto, F., Busser, C., Faestermann, T., Hain, K., Koll, D., Korschinek, G., Kraft, S., Ludwig, P., Plaschke, M., Schäfer, T., Geckeis, H., 2019. Ultratrace determination of 99TC in small natural water samples by accelerator mass spectrometry with the gas-filled analyzing magnet system. Anal. Chem. 91, 4585–4591.

Reiche, T., Noseck, U., Schäfer, T., 2016. Migration of Contaminants in Fractured-Porous Media in the Presence of Colloids: Effects of Kinetic Interactions. Transp. Porous Media 111, 143–170.

Reinhardt, M., Jacob, A., Sadeghnejad, S., Cappuccio, F., Arnold, P., Frank, S., Enzmann, F., Kersten, M., 2022. Benchmarking conventional and machine learning segmentation techniques for digital rock physics analysis of fractured rocks. Environ. Earth Sci. 81, 1–20.

Reinholdt, M., Miehe-Brendle, J., Delmotte, L., Tuilier, M.H., le Dred, R., Cortes, R., Flank, A.M., 2001. Fluorine route synthesis of montmorillonites containing Mg or Zn and characterization by XRD, thermal analysis, MAS NMR, and EXAFS spectroscopy. Eur. J. Inorg. Chem. 2831–2841.

Rinderknecht, F., 2017. Bentonite erosion and Colloid Mediated Transport of Radio-Nuclides in Advection Controlled Systems (in English). Faculty of Chemistry and Biosciences. Karlsruhe Institute of Technology (KIT), Karlsruhe.

Sadeghnejad, S., Enzmann, F., Kersten, M., 2021. Digital rock physics, chemistry, and biology: challenges and prospects of pore-scale modelling approach. Appl. Geochem. 131, 105028.

Sadeghnejad, S., Reinhardt, M., Enzmann, F., Arnold, P., Brandstätter, B., Wilde, F., Hupfer, S., Schäfer, T., Kersten, M., 2023. Minkowski functional evaluation of representative elementary volume of rock microtomography images at multiple resolutions. Adv. Water Resour. 104501.

Sánchez, L., Cuevas, J., Ramírez, S., Riuiz De León, D., Fernández, R., Vigil Dela Villa, R., Leguey, S., 2006. Reaction kinetics of FEBEX bentonite in hyperalkaline conditions resembling the cement–bentonite interface. Appl. Clay Sci. 33, 125–141.

Sanders, J., Fabian, A., Russell, H., Walker, S., Blundell, K., 2016. Detecting edges in the X-ray surface brightness of galaxy clusters. Mon. Not. R. Astron. Soc. 460, 1898–1911.

Sandić-Stanković, D.D., Kukolj, D.D., Le Callet, P., 2022. Quality assessment of DIBR-synthesized views based on sparsity of difference of closings and difference of Gaussians. IEEE Trans. Image Process. 31, 1161–1175.

Schäfer, T., Huber, F., Seher, H., Missana, T., Alonso, U., Kumke, M., Eidner, S., Claret, F., Enzmann, F., 2012. Nanoparticles and their influence on radionuclide mobility in deep geological formations. Appl. Geochem. 27, 390–403.

Schäfer, T., Pingel, J., Frank, T., Noseck, U., Seher, H., Geckeis, H., Kouhail, Y., Quinto, F., Schneeberger, R., 2023. In-Situ Experiments on Bentonite Long-Term Stability and Radionuclide Mobility at the Bentonite–Crystalline Interface at Grimsel Test Site. Nagra Technical Report NTB 23-10, Wettingen.

Scherbaum, F.J., Knopp, R., Kim, J.I., 1996. Counting of particles in aqueous solutions by laser-induced photoacoustic breakdown detection. Appl. Phys. B-Lasers Opt. 63, 299–306.

Schlickenrieder, L., Lanyon, G.W., Kontar, K., Blechschmidt, I., 2017. Grimsel Test Site Investigation Phase VI:Colloid Formation and Migration Project: Site Instrumentation and Initiation of the Long-Term In-Situ Test Nagra Technical Report 15-03. Wettingen (CH).

Schneeberger, R., Kober, F., Lanyon, G.W., Mäder, U.K., Spillmann, T., Blechschmidt, I., 2019. Grimsel Test Site: Revisiting the Site-Specific Geoscientific Knowledge. Nagra Technical Report 19-01. Wettingen (CH).

Seher, H., Geckeis, H., Fanghänel, T., Schäfer, T., 2020. Bentonite nanoparticle stability and the effect of fulvic acids: experiments and modelling. Colloids Interfaces 4, 16.

Sellin, P., Leupin, O.X., 2013. The use of clay as an engineered barrier in radioactive-waste management - a review. Clay Clay Miner. 61, 477–498.

Sertcelik, I., Kafadar, O., 2012. Application of edge detection to potential field data using eigenvalue analysis of structure tensor. J. Appl. Geophys. 84, 86–94.

Sharr, M.B., Parrish, C.E., Jung, J., 2024. Automated classification of valid and invalid satellite derived bathymetry with random forest. Int. J. Appl. Earth Obs. Geoinf. 129, 103796.

SKB, 2011. Long-term safety for the final repository for spent nuclear fuel at Forsmark: Main report of the SR-Site project, Updated 2015-05. Technical Report TR-11-01, Svensk Kärnbränslehantering AB.

Sommer, C., Straehle, C., Koethe, U., Hamprecht, F.A., 2011. Ilastik: Interactive learning and segmentation toolkit. In: 2011 IEEE International Symposium on Biomedical Imaging: From Nano to Macro. IEEE, pp. 230–233.

Stoll, M., Huber, F.M., Schill, E., Schäfer, T., 2017. Parallel-plate fracture transport experiments of nanoparticulate illite in the ultra-trace concentration range investigated by Laser-Induced Breakdown Detection (LIBD). Colloids Surf. A Physicochem. Eng. Asp. 529, 222–230.

Stoll, M., Huber, F.M., Trumm, M., Enzmann, F., Meinel, D., Wenka, A., Schill, E., Schäfer, T., 2019. Experimental and numerical investigations on the effect of fracture geometry and fracture aperture distribution on flow and solute transport in natural fractures. J. Contam. Hydrol. 221, 82–97.

Tang, K., Da Wang, Y., Mostaghimi, P., Knackstedt, M., Hargrave, C., Armstrong, R.T., 2022. Deep convolutional neural network for 3D mineral identification and liberation analysis. Miner. Eng. 183, 107592.

Tian, J., Qi, C., Sun, Y., Yaseen, Z.M., Pham, B.T., 2021. Permeability prediction of porous media using a combination of computational fluid dynamics and hybrid machine learning methods. Eng. Comput. 37, 3455–3471.

Torres, E., Turrero, M.J., Moreno, D., Sánchez, L., Garralón, A., 2017. FEBEX in-situ test: preliminary results of the geochemical characterization of the metal/bentonite interface. Proc. Earth Planet. Sci. 17, 802–805.

Tsai, W.-H., 1985. Moment-preserving thresolding: a new approach. Comput. Vis. Graph. Image Process. 29, 377–393.

Urazmatov, T., Iskandarov, S., Nurmetova, B., Gulomov, A., Khamraeva, S., Otamuratov, K., 2024. Development of an algorithm for extracting features in images based on the gabor filter. In: 2024 IEEE 3rd International Conference on Problems of Informatics, Electronics and Radio Engineering (PIERE). IEEE, pp. 1500–1505.

Villar, M.V., Martin, P.L., Pelayo, M., Ruiz, B., Rivas, P., Alonso, E., Lloret, A., Pintado, X., Gens, A., Linares, J., Huertas, F., Caballero, E., Jimenz de Cisneros, C., Obis, J., Perez, A., Velasco, J., 1998. FEBEX Bentonite: Origin, Properties and Fabrication of Blocks (Full-Scale Engineered Barriers Experiment in Crystalline Host Rock). ENRESA (Empresa Nacional De Residuos Radiactivos, S.A.), Madrid, Spain.

Vincent, L., Soille, P., 1991. Watersheds in digital spaces: an efficient algorithm based on immersion simulations. IEEE Trans. Pattern Analys. Mach. Intell. 13, 583–598.

Wang, S., Haralick, R.M., 1984. Automatic multithreshold selection. Comput. Vis. Graph. Image Process. 25, 46–67.

Yu, J., Huang, D., Wei, Z., 2018. Unsupervised image segmentation via stacked denoising auto-encoder and hierarchical patch indexing. Signal Process. 143, 346–353.